Article

Analysis of Error and Stability of Nanofluid over Horizontal Channel with Heat/Mass Transfer and Nonlinear Thermal Conductivity

Zeeshan [1],[†] , N. Ameer Ahammad [2], Nehad Ali Shah [3],[*],[†], Jae Dong Chung [3] , Attaullah [4]
and Haroon Ur Rasheed [5]

1   Department of Mathematics and Statistics, Bacha Khan University, Charsadda 24420, KP, Pakistan
2   Department of Mathematics, Faculty of Science, University of Tabuk, Tabuk 71491, Saudi Arabia
3   Department of Mechanical Engineering, Sejong University, Seoul 05006, Republic of Korea
4   Department of Mathematics, Abdul Wali Khan University, Mardan 25000, KP, Pakistan
5   Department of Computer Science and IT, Sarhad University, Peshawar 25000, KP, Pakistan
*   Correspondence: nehadali199@sejong.ac.kr
†   These authors contributed equally to this work and are co-first authors.

Abstract: The current investigation aims to analyze the nanofluid flow between two infinite rotating horizontal channels. The lower plate is porous and stretchable. The impact of physical parameters such as Hall current, thermal characteristics, heat source/sink, chemical reaction on velocity, temperature, and concentration profiles are discussed through graphs. The governing equations are transformed to ordinary differential equations using suitable transformations and then solved numerically using the RK4 approach along with the shooting technique. For varying values of the Schmidt number (SN) and the chemical reaction factor (CRF), the concentration profile declines, but decreases for the activation energy. It is observed that the velocity profile declines with the increasing values of the suction factor. The velocity profile increases when the values of the rotation factors are increased. The temperature field exhibits a rising behavior with increasing values of the thermophoresis factor, Brownian motion, and the thermal radiation factor. It is also observed that the heat transfer rate is significant at the lower wall with the increasing values of the Prandtl number (PN). For the numerical solution, the error estimation and the residue error are calculated for the stability and confirmation of the mathematical model. The novelty of the present work is to investigate the irregular heat source and chemical reaction over the porous rotating channel. A growing performance is revealed by the temperature field, with the increase in the Brownian motion (BM), thermophoresis factor (TF), thermal conductivity factor (TCF), and the radiation factor (RF).

Keywords: RK4 method; nanofluid; chemical reaction; heat/mass transfer; residue error; nonlinear thermal radiation; thermophoresis number; Brownian number; infinite vertical plates

MSC: 76D05; 76-10

1. Introduction

Nanofluid technology development is a very important topic of study in mathematics, manufacturing, physics and materials science [1]. Architects and researchers strive to effectively convey adequate understanding about the heat transfer process in nanofluids for most applications of practical interest. Nanofluids are critical in a wide range of applications, including chips, refrigerators, hybrid-powered motors, food improvement, heat exchangers and others. To enhance the thermal conductivity of the base fluid, such as water, ethylene, etc., the nanoparticles, for example, copper, aluminum, and carbon nanotubes, are suspended in the base fluid. The work of Buongiorno [2] gave a mathematical form of the nanoparticles and determined that, via basic mechanisms, it permits us with prodigious suppleness to enlighten the thermal features. Subsequently, mathematicians and

researchers widely used nanofluid to examine practical problems, such as industrial applications [3,4], biomedical engineering [5], solar thermal applications [6], and to numerous other production fields applying to different physical problems [7–9].

A few ongoing investigations have focused on different properties of nanoparticles used for different purposes. Sandeep et el. [10] investigated the MHD stagnation point movement over a stretching sheet. Sandeep et al. [11] examined the MHD flow with a heat source and thermal radiation. The hybrid nanofluid for heat enhancement passed through a stretched surface was studied by Samrat et al. [12]. Chalavadi et al. [13] showed the impact of the variable heat effect on the MHD Sakiadis movement over a continuous needle containing hybrid nanofluid. Despite the wide variety of applications for conventional fluids, several researchers found it difficult to achieve a satisfactory thermal performance [14–16]. Nehad et al. [17] investigated the thermodynamic activity of nanofluid flow through a vertical surface. This difficulty has challenged scientists to design a new class of nanoparticles that demonstrate noteworthy improvements in heat transmission in base fluids [18]. The hybrid nanofluid technique is used here to further develop an advanced nanofluid. This technique includes amalgam nanoparticles, which significantly enhance thermal conductivity in several applications compared to conventional fluids [19–22]. Hybrid nanofluid for different purposes includes solar energy, refrigeration, warming, power age, compound cycles, ventilation, and cooling. In recent years, there has been a tremendous increase in the research into hybrid nanoliquids for the foremost practical issues in a variety of sectors, particularly heat absorbers and electrical devices [23–27], and in several fields to attain an enhanced rate of heat transfer and thermal proficiency. A three-dimensional HN flow with varying thickness using the Cattaneo–Christov (C–C) model was investigated by Zhang et al. [28]. Saima et al. [29] inspected the squeezing HN flow among two surfaces with the same center towards varying thermal conductivity. Zeeshan et al. [30–32] distributed a mathematical description of a hybrid nanofluid (HN). Sohail et al. [33] inspected the HN flow over extending porous walls for unsteady, incompressible fluid with thermal characteristics. Recently, a few relevant studies have been published in [34–38]. Heat transfer happens due to temperature differences between dissimilar or the same bodies, according to the law of physics. It is interesting to note that FL (Fourier law) was considered a standard for heat diffusion, but it was later observed that this is not valid in many cases due to the initial disturbance that occurs during the practice. Cattaneo [39] determined this by signifying the addition of the thermal relaxation factor in the Fourier model. This was monitored by Christov [40], who recommended replacing the OUCD with respect to time. This altered version [41] is known as the C–C heat flux model. The C–C is used for many purposes, such as heat conduction, milk purification, and medical apparatus. Zeeshan et al. [42] explored an investigation communication by analyzing the Maxwell model flow above a stretchable sheet with C–C enclosing the slip effect by using the HAM approach. This innovative effort was tracked by Zeeshan et al. [43] taking a similar model over a sheet with changing thickness. In an alternative examination, Zeeshan et al. [44] used the same idea and considered the Oldroyd-8 model in place of Maxwell. The velocity of non-Newtonian viscous fluid affected by the magnetic field (MHD) was examined past an upright stretched sheet enclosing a C–C heat flux by Li et al. [45]. In fact, various fluid models are used with C–C heat flux in different geometries [46–52]. This sensation is witnessed and is also used in current studies [53,54].

The studies mentioned above demonstrate that a noteworthy amount of effort on liquid dynamics in a spinning horizontal tube can be cited. The investigation of micropolar fluid flow in a spinning duct inspired by chemical change and activation energy is rare and unexplored in research. The combination of Hall currents and linear radiant energy enhances the uniqueness of the original problem. The motion is examined with variable thermal and heat reservoirs. Using an appropriate similar conversion, the equations describing the mathematical model are transformed into ordinary differentials (ODEs). Furthermore, by introducing new variables, the ODEs are transformed to first-order nonlinear coupled differential equations then solved by RK4, a built-in function in MATLAB. The

outcomes of various parameters are inspected using tabular and graphical representation. The novelty of the present work is to investigate the irregular heat source and chemical reaction over the porous rotating channel. A growing performance is revealed by the temperature on growing the Brownian motion (BM), thermophoresis factor (TF), thermal conductivity factor (TCF), and radiation factor (RF). The present work is validated by previous work [55], and a good correspondence is found.

2. Mathematical Modeling

Consider infinite horizontal parallel disks in which the incompressible laminar flow of nanomaterial fluid is examined. The plates are porous and rotating with angular velocity $\Omega = (0, \Omega_1, 0)$ along the *y-axis*. The influence of the Hall current and thermal radiation is also considered. The Brownian motion and thermophoresis are characterized by the nanofluid model. The framework of the Cartesian coordinate system has been used to determine the problem's geometry, in which the *x-axis* is analogous to the disc, the *y-axis* is normal, and the *z-axis* is transverse to the *xy*-plane. The flow geometry is represented in Figure 1. When a consistent magnetic flux is pragmatic, the fluid becomes electrically conductive. The lower plate is elongated linearly $u_w = cx$ in the *x*-direction at $y = 0$, while the top plate is at $y = h$. The lower plate suctions fluid at $v = -v_0 (v_0 > 0$ correlates to suction, while $v_0 < 0$ refers to injection).
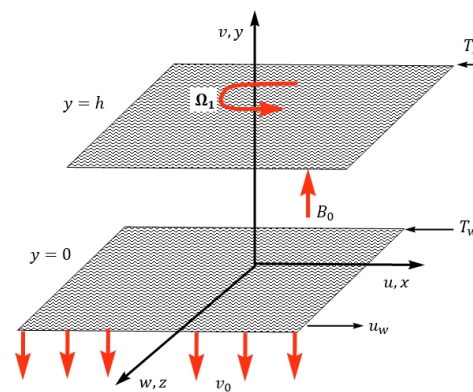

Figure 1. Flow geometry of the model.

The basic flow equations of nanofluid are [2,3,44,54]:

$$\frac{\partial \widetilde{u}}{\partial x} + \frac{\partial \widetilde{v}}{\partial y} \tag{1}$$

$$\widetilde{u}\frac{\partial \widetilde{u}}{\partial x} + \widetilde{v}\frac{\partial \widetilde{u}}{\partial y} + 2\Omega_1 \widetilde{w} = -\frac{1}{\rho}\frac{\partial \rho}{\partial x} + \nu\left(\frac{\partial^2 \widetilde{u}}{\partial x^2} + \frac{\partial^2 \widetilde{u}}{\partial y^2}\right) + \frac{\sigma_1 B_0^2}{\rho(1+m^2)}(\widetilde{u} - m\widetilde{w}), \tag{2}$$

$$\widetilde{u}\frac{\partial \widetilde{v}}{\partial x} + \widetilde{v}\frac{\partial \widetilde{v}}{\partial y} = -\frac{1}{\rho}\frac{\partial \rho}{\partial y} + \nu\left(\frac{\partial^2 \widetilde{v}}{\partial x^2} + \frac{\partial^2 \widetilde{v}}{\partial y^2}\right), \tag{3}$$

$$\widetilde{u}\frac{\partial \widetilde{w}}{\partial x} + \widetilde{v}\frac{\partial \widetilde{w}}{\partial y} - 2\Omega_1 \widetilde{u} = \nu\left(\frac{\partial^2 \widetilde{w}}{\partial x^2} + \frac{\partial^2 \widetilde{w}}{\partial y^2}\right) - \frac{\sigma_1 B_0^2}{\rho(1+m^2)}(m\widetilde{u} + \widetilde{w}), \tag{4}$$

$$\widetilde{u}\frac{\partial \widetilde{T}}{\partial x} + \widetilde{v}\frac{\partial \widetilde{T}}{\partial y} = \frac{1}{\rho C_P}\frac{\partial}{\partial y}[k(T)\frac{\partial \widetilde{T}}{\partial y}] + \tau[D_B \frac{\partial \widetilde{C}}{\partial y}\frac{\partial \widetilde{T}}{\partial y} + \frac{D_T}{\widetilde{T}_l}\left(\frac{\partial \widetilde{T}}{\partial y}\right)^2] - \frac{1}{\rho c_p}\frac{\partial q_r}{\partial y} + \frac{K(T)u_w}{xv\rho c_p}[D\left(\widetilde{T}_w - \widetilde{T}_l\right)f' + H\left(\widetilde{T} - \widetilde{T}_l\right)], \tag{5}$$

$$\widetilde{u}\frac{\partial \widetilde{C}}{\partial x} + \widetilde{v}\frac{\partial \widetilde{C}}{\partial y} = D_B[\frac{\partial^2 \widetilde{C}}{\partial x^2} + \frac{\partial^2 \widetilde{C}}{\partial y^2}] + \frac{D_T}{\widetilde{T}_l}\left(\frac{\partial^2 \widetilde{T}}{\partial x^2} + \frac{\partial^2 \widetilde{T}}{\partial y^2}\right) - k_r^2\left(\widetilde{C} - \widetilde{C}_l\right)\left(\frac{\widetilde{T}}{\widetilde{T}_l}\right)^n exp\left(\frac{-E_a}{k\widetilde{T}}\right) \tag{6}$$

With boundary conditions [4,43–45]:

$$\tilde{u}\Big|_{y=0} = u_w = cx, \tilde{v}\Big|_{y=0} = -v_0, \tilde{w}\Big|_{y=0} = 0, \tilde{T}\Big|_{y=0} = \tilde{T}_w, \tilde{C}\Big|_{y=0} = \tilde{C}_w \tag{7}$$

$$\tilde{u}\Big|_{y=h} = 0, \tilde{v}\Big|_{y=h} = 0, \tilde{w}\Big|_{y=h} = 0, \tilde{T}\Big|_{y=h} = \tilde{T}_l, \tilde{C}\Big|_{y=h} = \tilde{C}_l.$$

The radioactive heat flux is expressed by the following relation [3,44]:

$$q_r = -\frac{4}{3}\frac{\partial T^4}{\bar{\bar{k}}}\frac{\partial T^4}{\partial y}, \text{ where } T^4 = 4T_l^3 T - 3T_l^4 \tag{8}$$

The varying thermal conductivity given in Equation (5) is explored as [46,47]:

$$K = k_0\left(1 + d\left(\frac{T - T_l}{T_w - T_l}\right)\right) \tag{9}$$

By using Equations (8) and (9), Equation (5) becomes:

$$\tilde{u}\frac{\partial \tilde{T}}{\partial x} + \tilde{v}\frac{\partial \tilde{T}}{\partial y} = \frac{1}{\rho C_P}\frac{\partial}{\partial y}\left[k_0(1+d\theta)\frac{\partial \tilde{T}}{\partial y}\right] + \tau\left[D_B\frac{\partial \tilde{C}}{\partial y}\frac{\partial \tilde{T}}{\partial y} + \frac{D_T}{\tilde{T}_l}\left(\frac{\partial \tilde{T}}{\partial y}\right)^2\right] + \frac{16}{3}\frac{T_l^3}{\bar{\bar{k}}}\frac{T_l^3}{\rho C_P}T\frac{\partial^2 T}{\partial y^2} + \frac{k_0(1+d\theta)u_w}{xv\rho c_\rho}\left[D\left(\tilde{T}_w - \tilde{T}_l\right)f' + H\left(\tilde{T} - \tilde{T}_l\right)\right], \tag{10}$$

By proper conversion [2,3,44]:

$$\tilde{u} = cxf'(\eta), \tilde{v} = -chf(\eta), \tilde{w} = cxj(\eta), \theta(\eta) = \frac{\tilde{T} - \tilde{T}_l}{\tilde{T}_w - \tilde{T}_l}, (\eta) = \frac{\tilde{C} - \tilde{C}_l}{\tilde{C}_w - \tilde{C}_l}, \eta = \frac{Y}{H}. \tag{11}$$

By using Equation (11), the Equation (1) satisfies automatically and Equations (2)–(4), (6), (7) and (10) yield the system:

$$\frac{d^4 f}{d\eta^4} = R_e\left(\frac{df}{d\eta}\frac{d^2 f}{d\eta^2} - f\frac{d^3 f}{d\eta^3}\right) + 2\alpha_1\frac{dj}{d\eta} - \frac{Ha^2}{(1+m^2)}\left(\frac{d^2 f}{d\eta^2} - m\frac{dj}{d\eta}\right), \tag{12}$$

$$\frac{d^2 j}{d\eta^2} = R_e\left(f\frac{dj}{d\eta} - f\frac{df}{d\eta}j\right) - 2\alpha_1\frac{df}{d\eta} + \frac{Ha^2}{(1+m^2)}\left(j + m\frac{df}{d\eta}\right), \tag{13}$$

$$\left((1+d\theta) + \frac{4}{3}Rd\right)R_e)\frac{d^2\theta}{d\eta^2} = -Pr\left(f\frac{d\theta}{d\eta} + R_e\left(Nb\frac{d\theta}{d\eta}\frac{d\phi}{d\eta} + Nt\left(\frac{d\theta}{d\eta}\right)^2\right)\right) - (1+d\theta)\left(D\frac{df}{d\eta} + H\frac{d\theta}{d\eta}\right) - R_e d\left(\frac{d\theta}{d\eta}\right)^2, \tag{14}$$

$$\frac{d^2}{d\eta^2} = -\frac{Nt}{Nb}\frac{d^2\theta}{d\eta^2} + Sc(\delta\phi\left(1 + \alpha\theta\right)^n exp\left(\frac{-E}{(1+\alpha\theta)}\right) - f.R_e\frac{d\phi}{d\eta}). \tag{15}$$

The boundary constraints take the form:

Lower plate : $\frac{df}{d\eta}(0) = 1, f(0) = K, j(0) = 0, \theta(0) = 1, \phi(0) = 1,$
Upper plate : $\frac{df}{d\eta}(1) = 0, f(1) = 0, j(1) = 0, \theta(1) = 0, \phi(1) = 0.$ $\tag{16}$

The physical quantities of interest are as follows:

$$C_{f,lower} = \frac{\mu}{\rho u_w^2}\frac{\partial u}{\partial y}\Big|_{y=0} \tag{17}$$

$$C_{f,upper} = \frac{\mu}{\rho u_w^2}\frac{\partial u}{\partial y}\Big|_{y=h} \tag{18}$$

$$Nu_{lower} = \frac{hQ_w}{k_0(T_w - T_l)}, Q_w = -k(T)\frac{\partial T}{\partial y} + qr\Big|_{y=0} \tag{19}$$

$$Nu_{upper} = \frac{hQ_w}{k_0(T_w - T_l)}, Q_w = -k(T)\frac{\partial T}{\partial y} + qr \Big|_{y=h} \tag{20}$$

$$Sh_{lower} = \frac{hQ_m}{D_{B(C_w - C_l)}}, Q_m = -D_B\frac{\partial C}{\partial y} \Big|_{y=0} \tag{21}$$

$$Sh_{lower} = \frac{hQ_m}{D_{B(C_w - C_l)}}, Q_m = -D_B\frac{\partial C}{\partial y} \Big|_{y=h} \tag{22}$$

Using Equation (11), Equations (17)–(22) are transformed into:

$$(Re_h C_f)_{flower} = \frac{d^2 f}{d\eta^2}\Big|_{\eta=0}, (Re_h C_f)_{upper} = \frac{d^2 f}{d\eta^2}\Big|_{\eta=1} \tag{23}$$

$$(Nu)_{lower} = -\left(1 + \left(\frac{4}{3}\right)\cdot\frac{Rd}{1+d\theta}\right)\frac{d\theta}{d\eta}\Big|_{\eta=0}, (Nu)_{upper} = -\left(1 + \left(\frac{4}{3}\right)\cdot\frac{Rd}{1+d\theta}\right)\frac{d\theta}{d\eta}\Big|_{\eta=1} \tag{24}$$

$$(Sh)_{lower} = -\frac{d\varphi}{d\eta}\Big|_{\eta=0}, (Sh)_{upper} = -\frac{d\varphi}{d\eta}\Big|_{\eta=1} \tag{25}$$

3. Numerical Procedure and Stability Analysis

The modeled equations are solved numerically by the RK4 scheme and the shooting technique. For this objective, the higher-order ODEs are converted to first order differential equations by introducing new variables. The set of equations along with the boundary constraint are solved with the help of RK4 and the shooting technique by taking step size $\Delta\eta = 0.01$ and tolerance 10^{-5}. This shows that our solution obtained by the RK4 built-in function in MATLAB is corrected and converges up to the five decimal places by ignoring the irregular heat source and chemical reaction, as reported by Tili et al. [55]. Table 1 provides the stability analysis of the current study with Tili et al. [55], and an outstanding agreement is found. The flow chart of the RK4 method is shown in Figure 2.

Table 1. Validation of the present work with published work for temperature and concentration profiles.

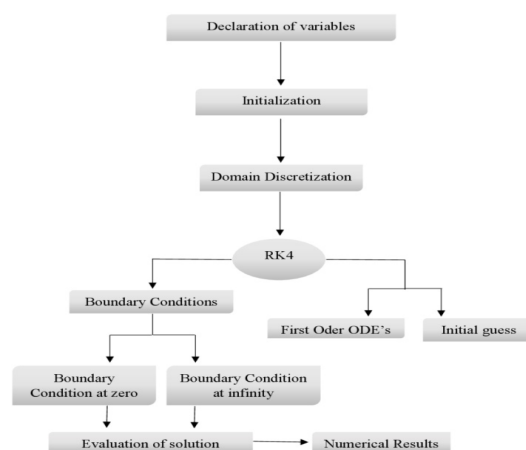| η	Tili et al. [55] $\theta(\eta)$	Current	Tili et al. [55] $\phi(\eta)$	Current
0	1	1	1	1
0.1	0.7568230	0.7568230	0.6160560	0.6160560
0.3	0.6071153	0.6071151	0.3736382	0.3736381
0.5	0.4046126	0.4046123	0.1671527	0.1671527
0.7	0.1718404	0.1718401	0.0026777	0.0026777
1	0	0	0	0

Figure 2. Flow chart of RK4 method.

4. Error Analysis and Confirmation of RK4 Method

For utmost differential equations, the outcomes given by RK4 are relatively accurate. Because its outcomes are established on numerical sampling and error estimates, there can rarely be significant errors. When you need to be assured of the excellence of a solution, it is worthwhile completing a basic inspection of the solution. Linking a solution computed with work precision higher than the default Machine Precision (MP) is often a convenient way to check consequences. Use RK4 with the default work precision to compute the problem's solution and then use the same method with working precision-22 to compute the error solution. On the basis of working precision to compute the problem solution with working precision-22, the residue error has been computed shown in the red and black lines in Figure 3. The black lines shows the large residue error while the red line shows small residue error which confirm the solution.
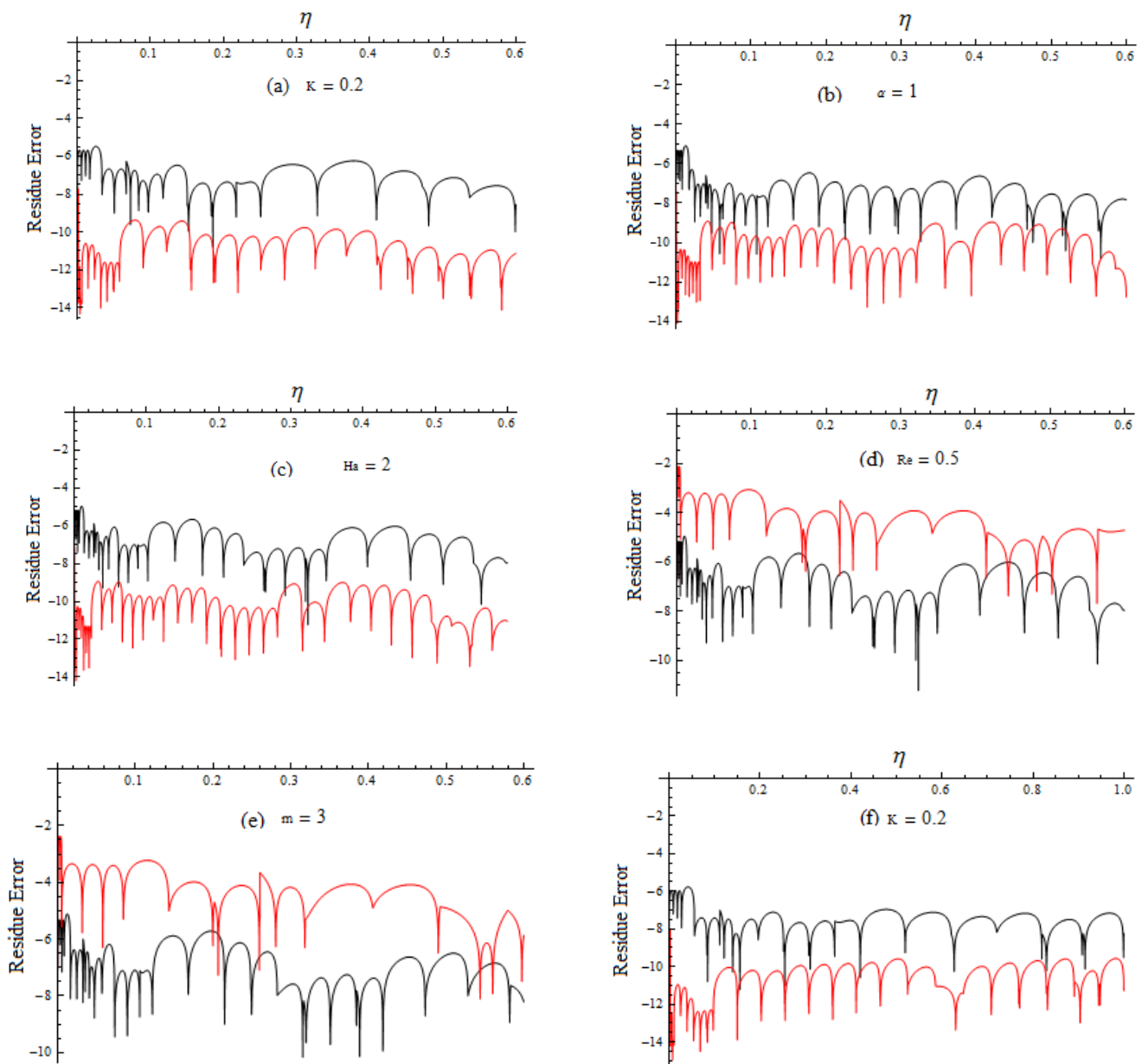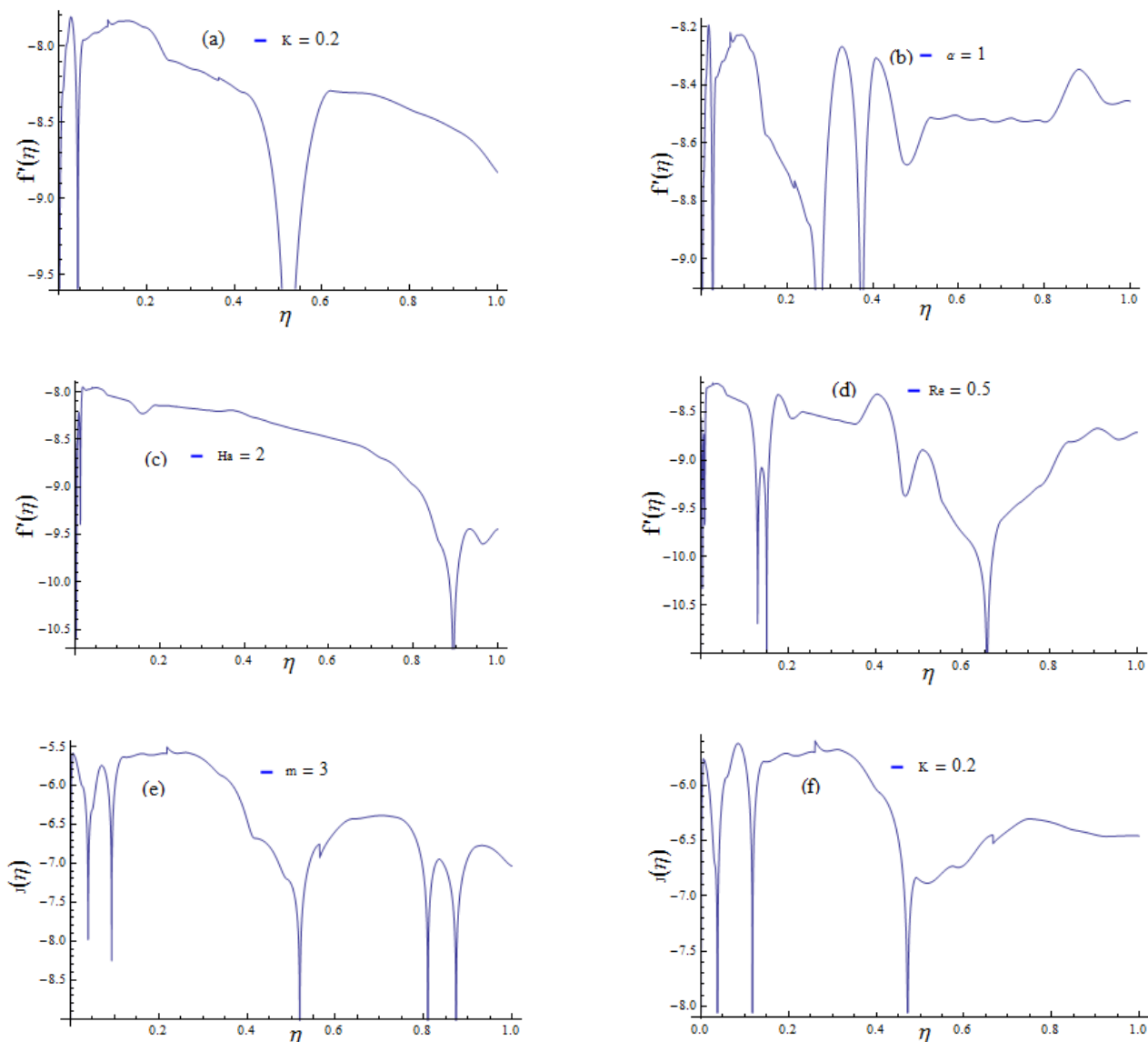

Figure 3. Residue Error analysis for different parameters on velocity profiles (**a**) K on $f'(\eta)$, (**b**) a on $f'(\eta)$, (**c**) Ha on $f'(\eta)$, (**d**) Re on $f'(\eta)$, (**e**) m on $J(\eta)$, (**f**) K on $J(\eta)$.

Subsequently, errors are frequently quite small; it is beneficial to interpret them on a logarithmic scale. Real exponent [x] is effectually equal to Log 10 (Abs [x]) but without a singularity at zero, so it is a good choice for viewing differences that might be zero at some points.

In the following graphs, we estimated the error solutions for different physical parameters involved in the model. From these figures, it is clear that our numerical solution is accurate as the error is too small. Figure 4a–f shows the error analysis of the physical parameters, *K*, *a*, *Ha*, and *Re* on $f'(\eta)$, and *m* and *K* on $J(\eta)$, respectively. From this figure, it is shown that our numerical computation is correct. Similarly, on the basis of working precision to compute the problem solution with working precision-22, the residue error has been computed shown in the red and black lines in Figure 3a–f. The black lines show the large residue error while the red line shows small residue error which confirms the solution.

Figure 4. Error analysis for different parameters on velocity profiles (**a**) *K* on $f'(\eta)$, (**b**) *a* on $f'(\eta)$, (**c**) *Ha* on $f'(\eta)$, (**d**) *Re* on $f'(\eta)$, (**e**) *m* on $J(\eta)$, (**f**) *K* on $J(\eta)$.

5. Results and Discussion

The nonlinear Equations (12)–(15) are solved numerically by using RK4 along with the shooting technique. The characteristics of the velocities $f'(\eta)$, $j(\eta)$, and temperature $\theta(\eta)$ and the concentration $\phi(\eta)$ for the non-dimensional variables arising in this study are

represented graphically. Figure 5a,b demonstrates the impression of changing the suction factor K on velocities. Since the lower plate sucked nanofluid, a large amount of fluid is ejected into the area around the lower plate. As a result, the velocities $f'(\eta)$ and $j(\eta)$ are decreased due to the increase in the suction factor. The effect of the rotation factor α on $f'(\eta)$ and $j(\eta)$ is seen in Figure 6a,b. The Coriolis force, which operates normally to the velocity profile and the rotating axis in a rotating channel, opposes the fluid movement. As a consequence, there is a two-fold impression for $f'(\eta)$. When α is strengthened, the velocity $f'(\eta)$ drops in the nearest region of the lower plate while increasing in the uppermost part of the channel. It is observed that as α increases, the velocity $j(\eta)$ decreases. Figure 7a,b shows the magnetic variable Ha impact on $f'(\eta)$ and $j(\eta)$. The Lorentz force, which opposes the fluid motion, increases with the increasing values of the magnetic factor. In Figure 7a, there is a decrease in $f'(\eta)$ before the midpoint of the network, but there is a boosting nature in the high half of the channel. It is shown that on altering Ha, the fluid movement starts to deteriorate, as shown in Figure 7b. Figure 8a,b demonstrate the impression of the Reynolds number Re, since the Reynolds number is the proportion of inertial to viscous forces. As a result, as Re improves, inertial forces improve, while viscous forces decrease. A two-fold influence is observed for $f'(\eta)$, but the velocity $j(\eta)$ decreases. Figure 9a,b demonstrate the behavior of the Hall current variable m on $f'(\eta)$ and $j(\eta)$. The effective conductivity $\frac{\sigma 1}{1+m^2}$ greatly diminishes when m is amplified. As a result, the magnetic damping force effect is significantly diminished. As seen in Figure 9a, the velocity of the fluid declines in the domain $0 \leq \eta \leq 0.4$ and increases in the $0.4 \leq \eta \leq 1$ of the channel. The fluid velocity $j(\eta)$ decreases as m increases. Figure 10 depicts the outcome of the thermophoresis variable Nt on $\theta(\eta)$. For increasing Nt values, nanoparticles travel from higher pressure to lower pressure fluid. It has been discovered that increasing Nt strengthens thermophoretic force. As a result, an increment in $\theta(\eta)$ is observed. Figure 11 highlights the inspiration of Nb on $\theta(\eta)$. It has been determined that significantly increasing Nb values lead to a significant heat gene ration due to nanoparticle collision. As a result, increases. Figure 12 portrays the influence of the radiation variable Rd, implying the radiation factor and the random motion of the nanoparticles increase, providing the additional energy inside the fluid. As a consequence, the temperature of the fluid is increased. Figure 13 explores the influence of thermal factor d on the temperature profile $\theta(\eta)$. The increment in d improves the random motion of nanoparticles, which increases the heat function and causes an increase in the temperature inside the fluid. Figure 14a,b and Figure 15a,b demonstrate the presentation of the variable heat source/sink on temperature $\theta(\eta)$. It is observed that increasing the amount of the variable heat source variable $(D > 0, H > 0)$ corresponds to significantly increased heat generation. As a result, the temperature increases. However, when the variable sink value $(D > 0, H > 0)$ is significantly changed, the nature of $\theta(\eta)$ deteriorates, owing to the inner absorption of heat. Figure 16 explores the influence of Schmidt number Sc on the concentrated field. It is perceived that by increasing Sc, the concentration field decreases, owing to a lessening in mass dissemination. Figures 17 and 18 show the effect of the Brownian motion Nb and thermophoresis variable Nt on concentration field $\phi(\eta)$. It is observed that $\phi(\eta)$ is declined with the increasing values of Nb and enhanced with the growing values of Nt. By increasing Nt, the random motion of nanoparticles improves, which enhances the concentration profile. Random mobility among the fluid molecules upsurges as Nb increases. In conclusion, by amplifying Nb, fluid concentration deteriorates. Figure 19 exhibits the outcome of the dimensionless chemical reaction parameter δ on $\phi(\eta)$. The chemical molecule diffusivity decreases as a result of reaction processes. As a result, the fluid concentration decreases. Figure 20 exhibits the influence of activation energy E values. It is observed that higher E values cause a reduction in the Arrhenius function. As a result, the chemical reaction decreases. As E is increased, so does the fluid concentration. Figure 21 depicts the outcome of the temperature difference of variable a_1 on $\phi(\eta)$. A poorer concentration profile is observed as the temperature difference (at the surface and far away from the surface) escalates. Similarly, the effect of physical parameters such as the magnetic parameter Ha, Schmidt number Sc, and Brownian motion parameters

Nb on the skin friction and the Sherwood number is depicted in Figures 22 and 23. From Figure 22, it is quite clear that the skin friction increases as the magnetic parameter increases. This is because when the magnetic field is applied, the Lorentz force is developed as a result. Due to this, the Lorentz skin friction increases. Similarly, the Sherwood number increases with the increasing values of Sc and Nb, as shown in Figure 23.
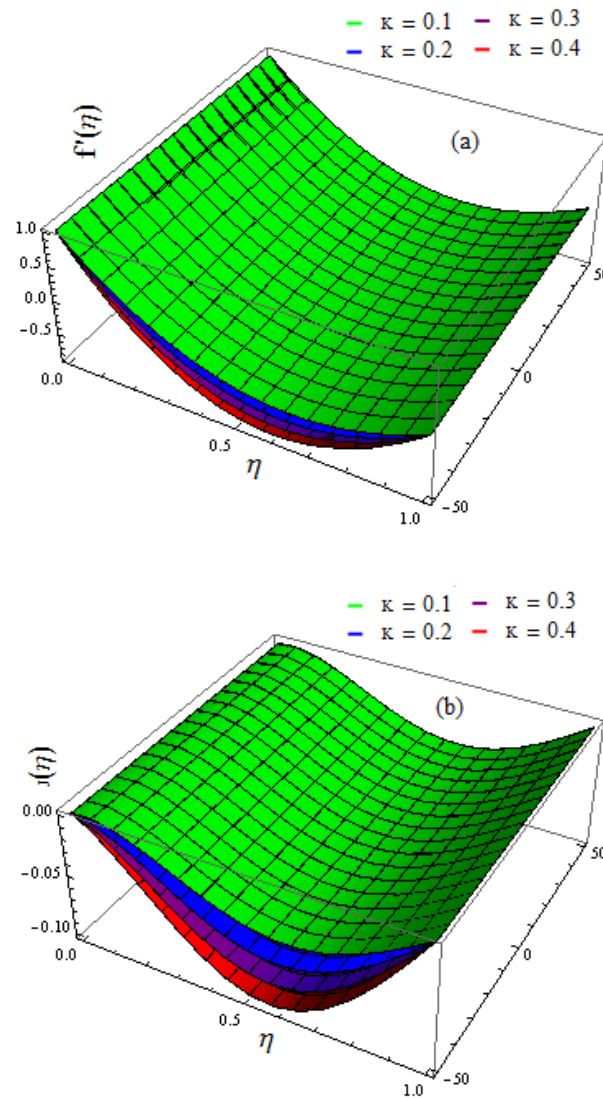

Figure 5. (**a**) Influence of K on $f'(\eta)$. (**b**) Influence of K on $J(\eta)$.
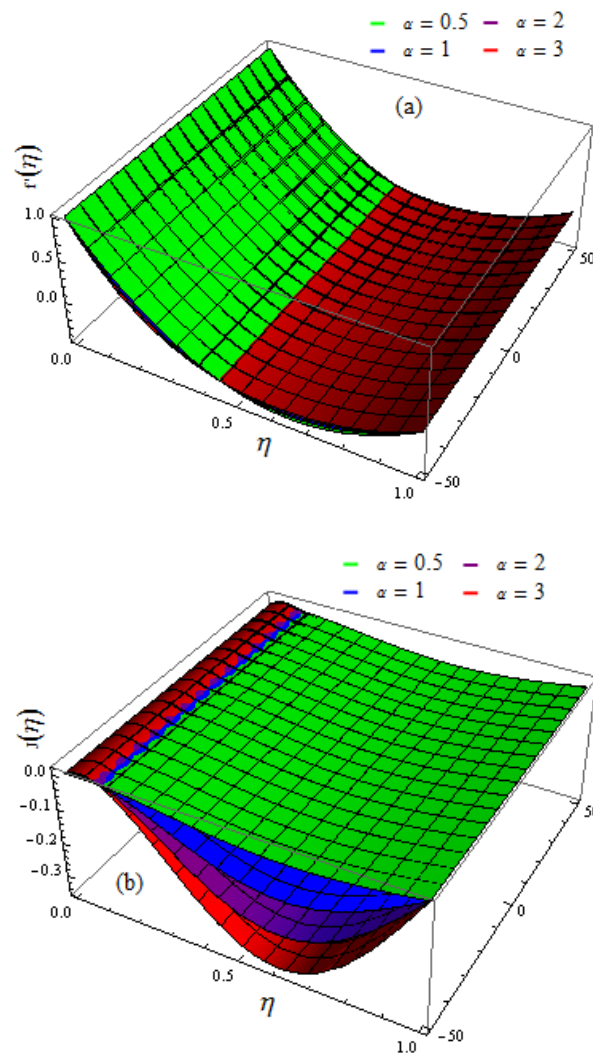
Figure 6. (**a**) Influence of *a* on $f'(\eta)$. (**b**) Influence of *a* on $J(\eta)$.
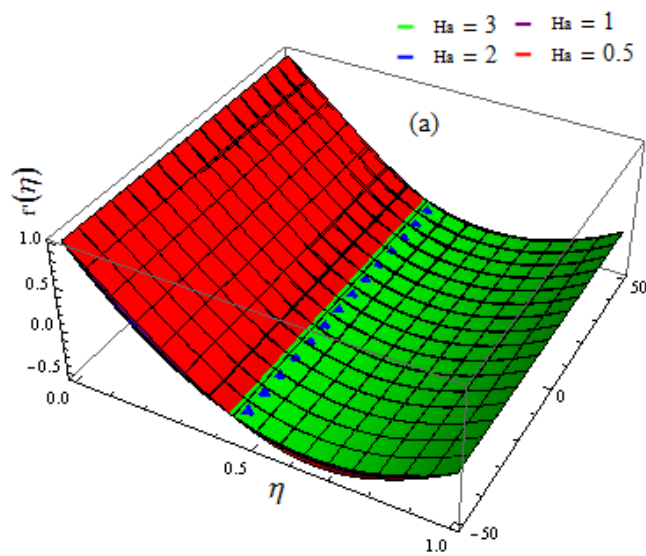
Figure 7. *Cont.*
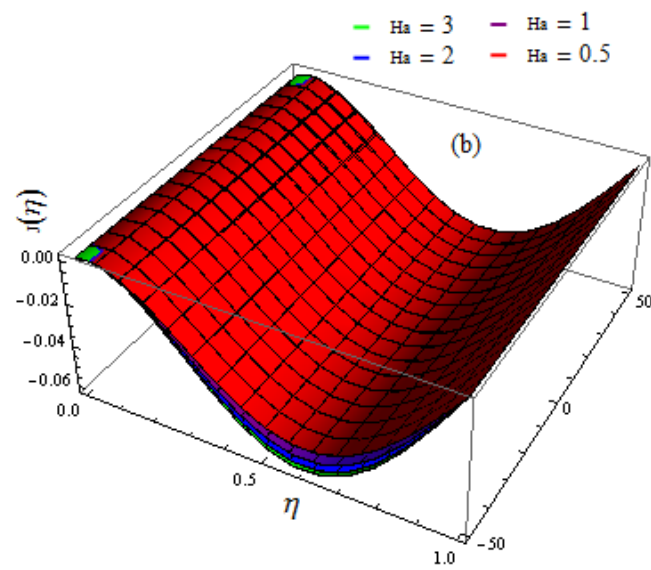
Figure 7. (**a**) Influence of Ha on $f'(\eta)$. (**b**) Influence of Ha on $J(\eta)$.
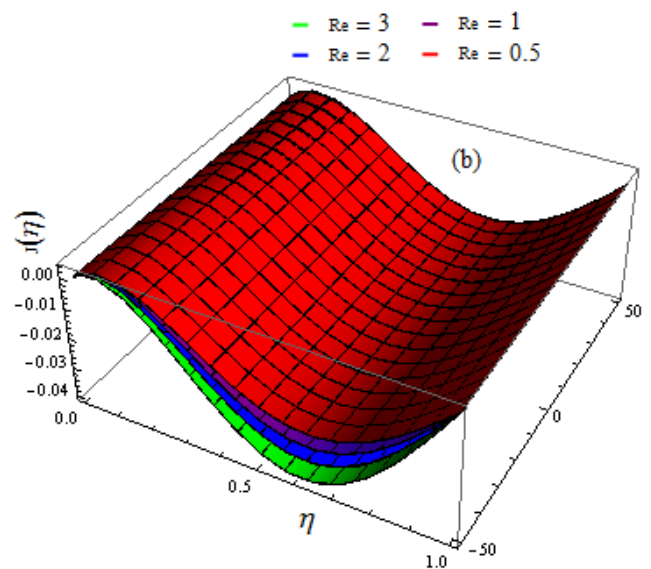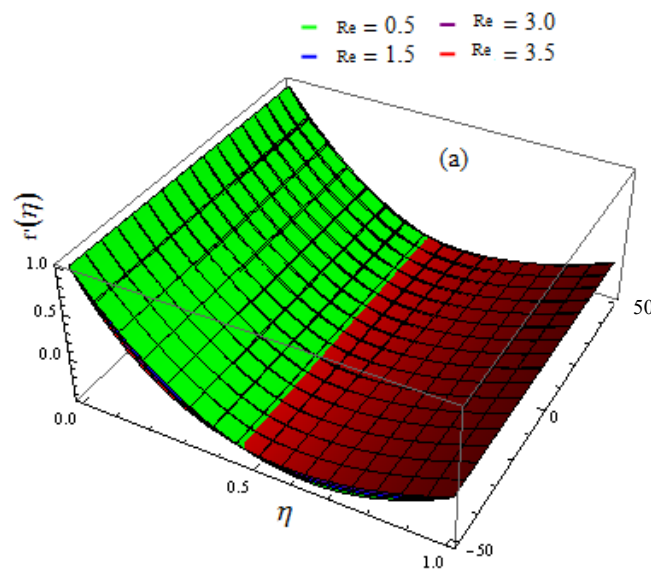
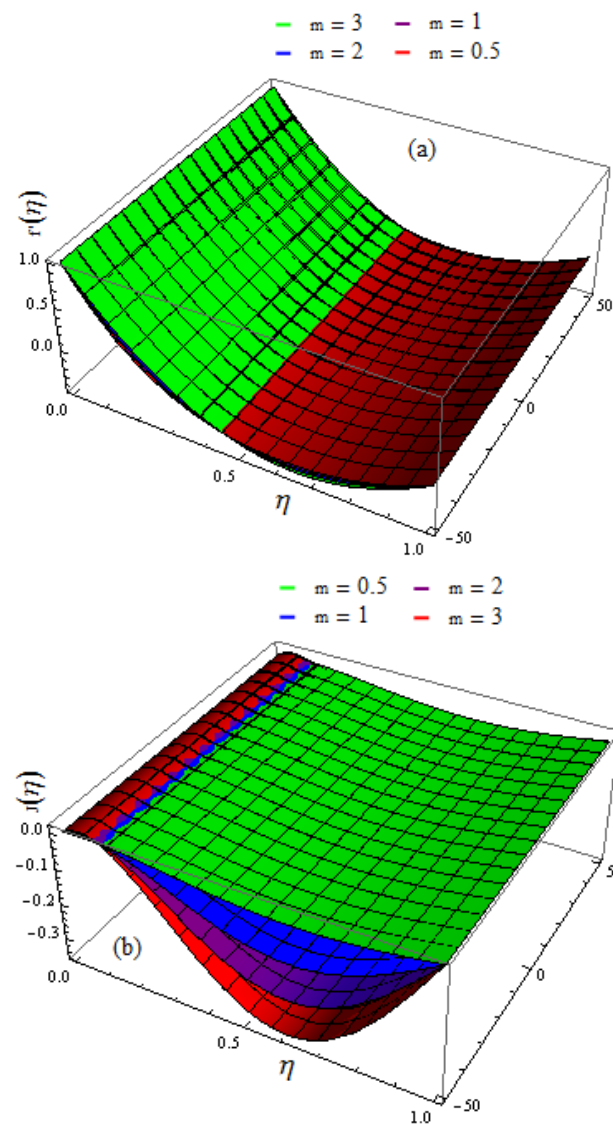**Figure 8.** (**a**) Influence of Re on $f'(\eta)$. (**b**) Influence of Re on $J(\eta)$.

Figure 9. (**a**) Influence of m on $f'(\eta)$. (**b**) Influence of m on $J(\eta)$.
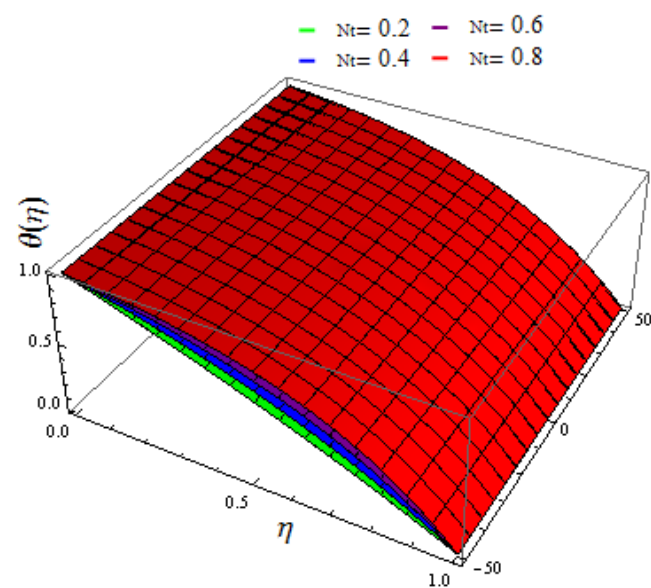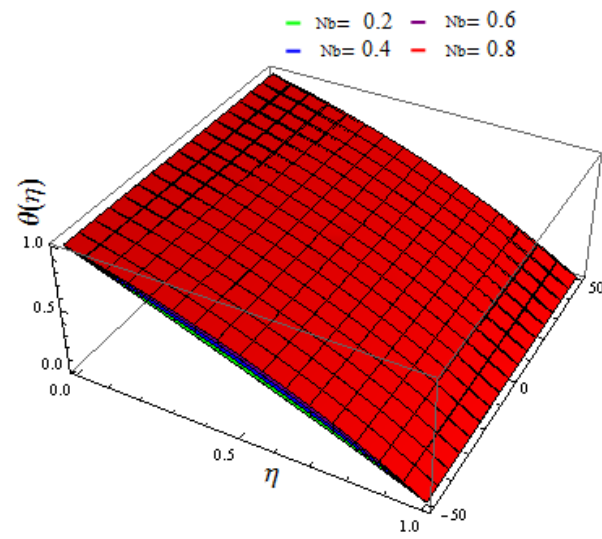

Figure 10. Impact of Nt on $\theta(\eta)$.

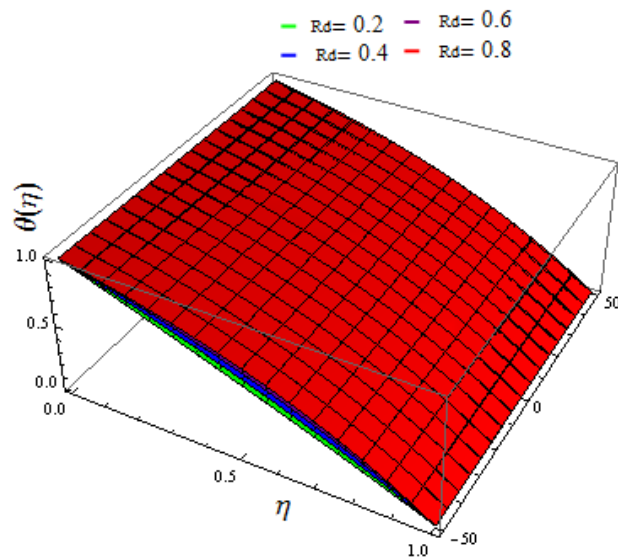**Figure 11.** Impact of Nb on $\theta(\eta)$.
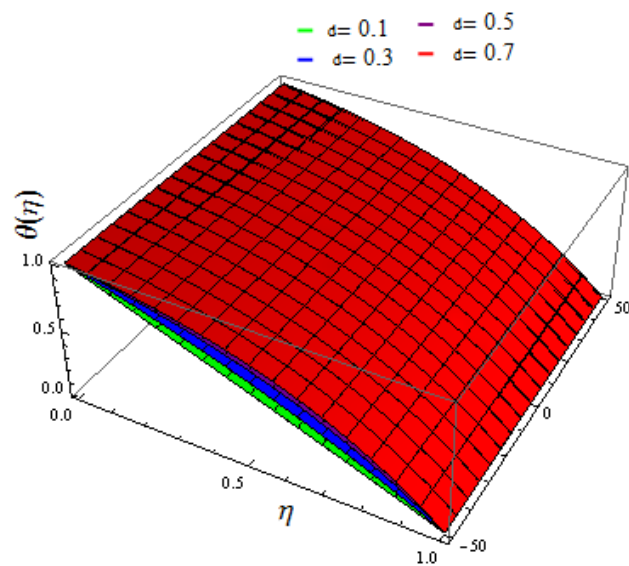

Figure 12. Impact of Rd on $\theta(\eta)$.
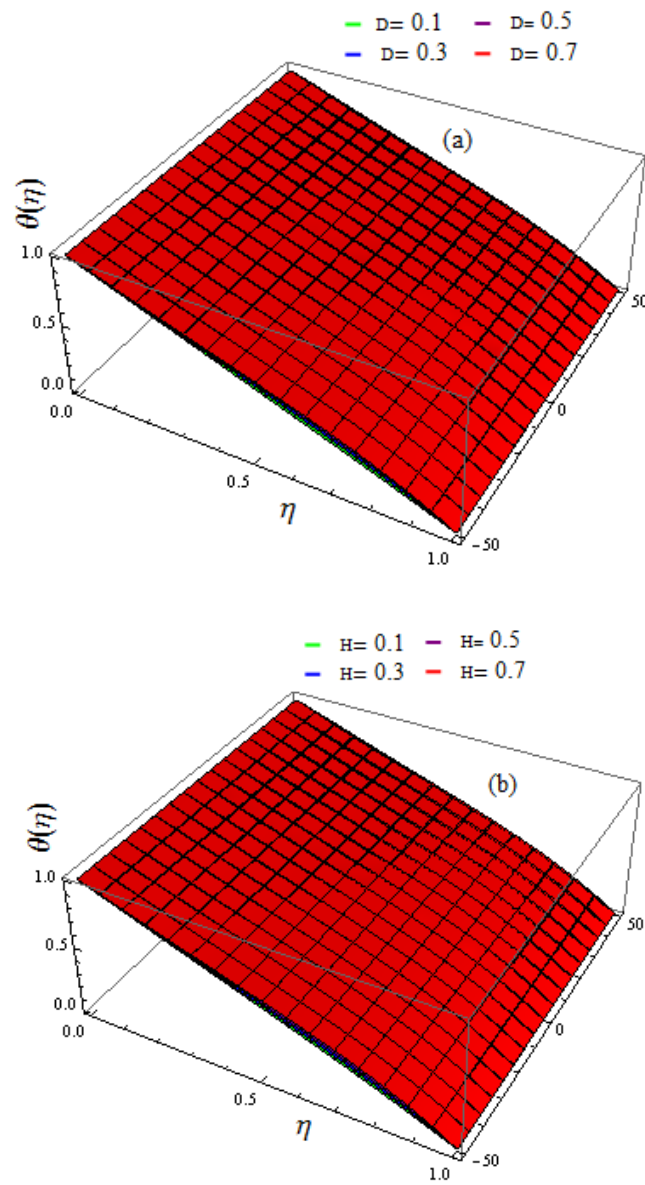

Figure 13. Impact of d on $\theta(\eta)$.

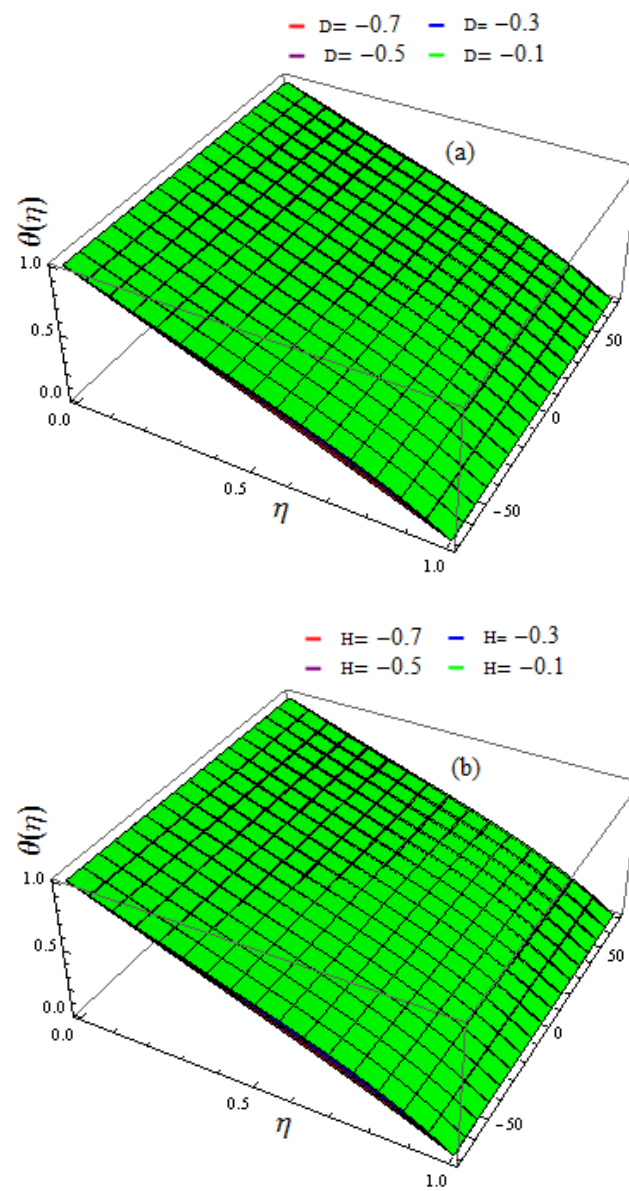**Figure 14.** (**a**) Impact of $D > 0$. (**b**) $H > 0$ on $\theta(\eta)$.

Figure 15. (**a**) Influence of $D < 0$. (**b**) $H < 0$ on $\theta(\eta)$.
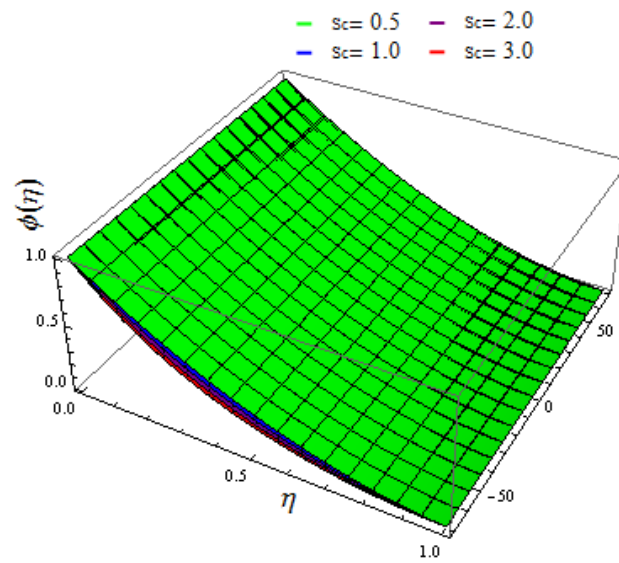
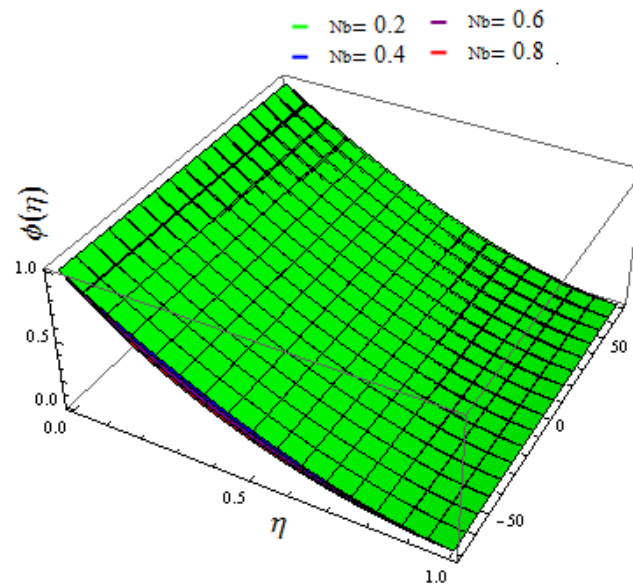**Figure 16.** Influence of Sc on $\phi(\eta)$.

Figure 17. Influence of Nb on $\phi(\eta)$.
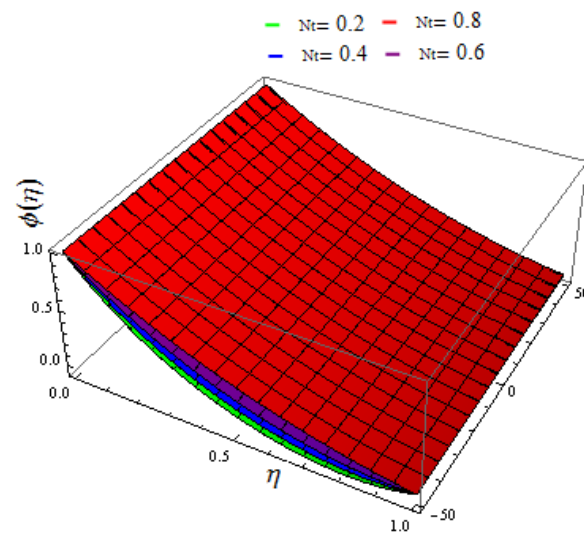
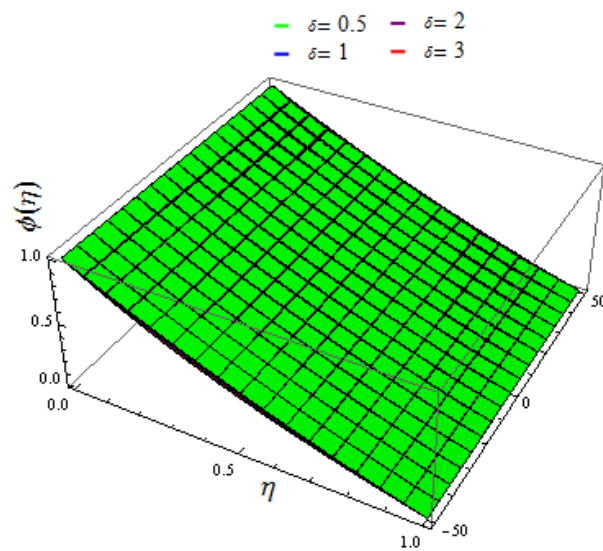**Figure 18.** Influence of Nt on $\phi(\eta)$.

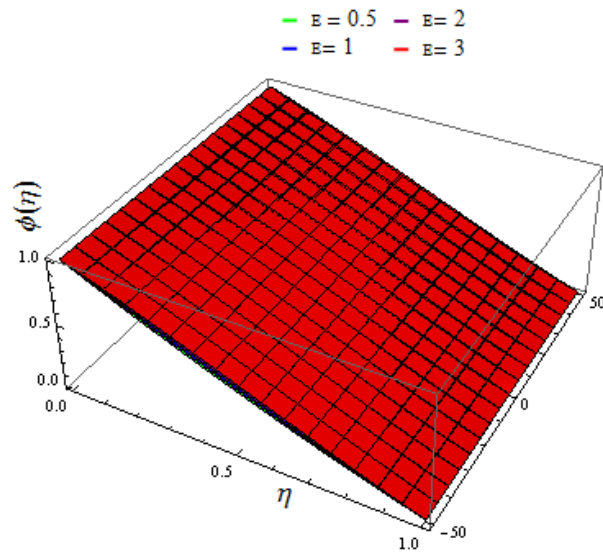**Figure 19.** Influence of δ on $\phi(\eta)$.

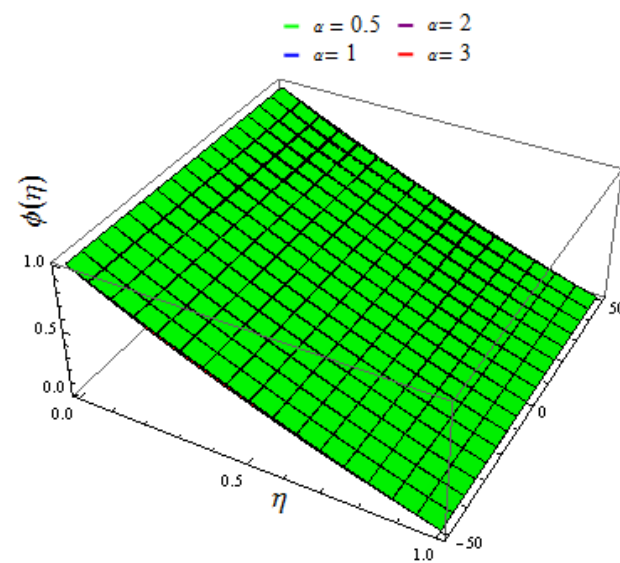**Figure 20.** Influence of E on $\phi(\eta)$.

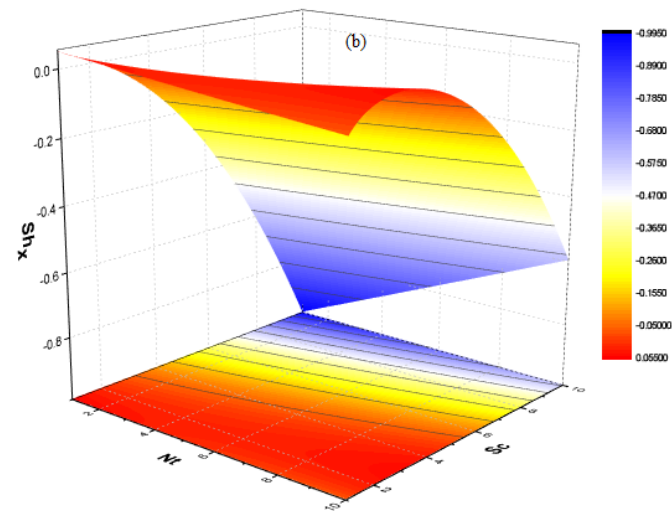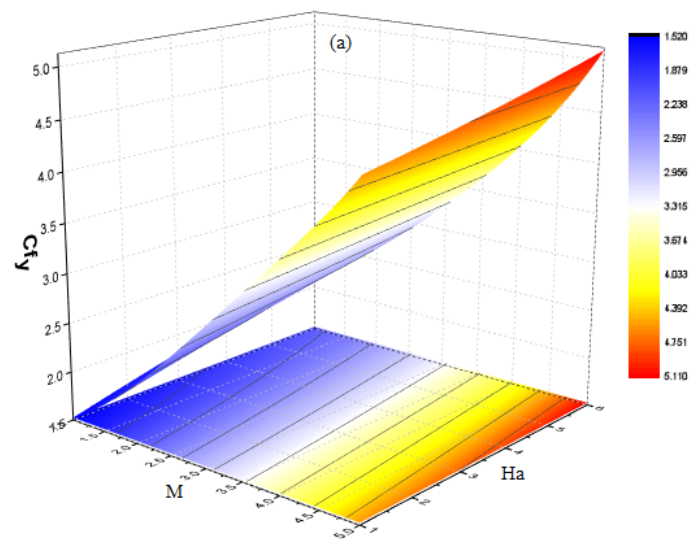**Figure 21.** Influence of a_1 on $\phi(\eta)$.

Figure 22. (**a**) Influence of *Ha* on skin friction. (**b**) Influence of *Sc* on Sherwood number.
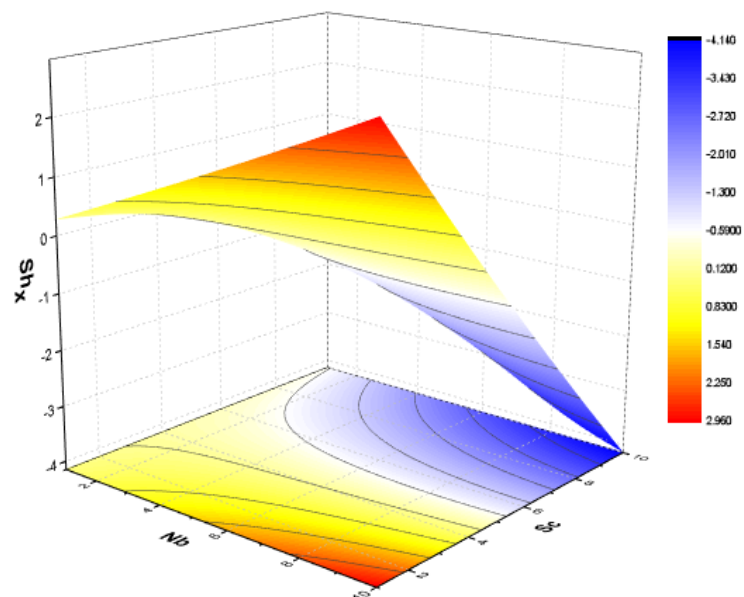

Figure 23. Impact of *NbandSc* on Sherwood number.

Table 2 investigates the effect of Ha, α, and K on shear stress at the lower and upper walls. It is witnessed that as Ha improves, shear stress increases at both walls, while when the value of K increases, $f''(0)$ and $j\prime(0)$ decrease, so far as the shear force at the top is increased. When the rotation variable is amplified, the shear stress at the upper wall is increased. However, for $f''(0)$, a reversed analysis is observed. Table 3 illustrates the inspiration of Pr, Rd, and d on the heat transmission rate. The heat transmission is observed to be increasing when Pr, Rd, and d values are increased. Table 4 shows the effect of various Sc, δ, E, Nt, and Nb values on the mass transfer rate. It is realized that as Sc and δ are enhanced, the mass transfer rate $\phi\prime(0)$ is increased at the bottom wall. However, $\phi\prime(0)$ decays with increasing E, Nt, and Nb values. The mass transfer rate decreases at the upper wall as Sc and δ are increased but enhances as the values of E, Nt, and Nb are increased.

Table 2. Numerical values for Friction Drag Coefficient at both walls.

Ha	α_1	K	$f''(0)$	$J'(0)$	$f'(1)$	$J'(1)$
0.4	1	0.2	−3.8262455	0.22541159	3.5926925	0.54849149
0.6			−3.7983194	0.22937296	3.5992994	0.58998432
0.8			−3.7619566	0.23142925	3.5987119	0.64987973
0.3	1	0.4	−3.7988799	0.28672762	3.5953999	0.97287839
	3		−3.9971633	0.37866375	3.6589899	1.5282953
	5		−4.4167316	0.43814944	3.7469865	1.9585998
0.4	1	0.1	−4.5444949	−0.1333518	3.9993977	0.67772693
		0.3	−5.9429682	−0.3575427	4.9899783	0.93912785
		0.5	−7.6632682	−0.5299198	5.9943565	1.1715158

Table 3. Numerical values for heat transfer rate.

Pr	Rd	d	$-(1+\frac{Rd}{1+d\theta})\theta'(0)$	$-(1+\frac{Rd}{1+d\theta})\theta'(1)$
1	0.5	0.2	2.9693338	3.3797674
4			3.1232217	3.4167495
7			3.1763599	3.6592875
3	0.2	0.1	2.6937456	2.9846985
	0.4		2.9717172	3.3412984
	0.6		3.2393369	3.5999498
3	0.5	0.2	3.1792415	3.6889439
		0.4	3.3259978	3.1497378
		0.6	3.4679672	4.6419175

Table 4. Numerical values for mass transfer rate.

Sc	Nt	δ	Nb	E	$-\phi'(0)$	$-\phi'(1)$
0.5	0.2	0.4	0.2	0.5	1.2682748	0.8782798
1.0					1.3569924	0.8331143
1.4					1.4471383	0.7999553
1.0	0.1				1.8912389	3.7326718
	0.3				1.7123892	3.9118486
	0.5				1.5379884	4.2974655
	0.1	0.6			1.2446956	0.8882515
		1.2			1.2747579	0.8771941
		1.4			1.2944949	0.8663445
			0.2		1.9955616	3.4693693
			0.4		1.6926893	3.9924682
			0.6		1.3628933	4.5733221
				1	1.1981187	0.8961844
				2	1.1853191	0.8999332
				3	1.1791132	0.9129878

6. Conclusions

A mathematical explanation for nanofluid flow between two infinite parallel channels is investigated numerically. The PDEs are converted to first ODEs by applying the new variables and solved by bvph2. The effect of physical parameters on the velocities, temperature, and concentration profiles are examined through graphs. The physical quantities of interest are also analyzed numerically through tables. The novelty of the present work is to investigate the irregular heat source and chemical reaction over the porous rotating channel. Tili et al. [55] investigated the thermodynamic analysis of MHD nanofluid in a porous channel with radiation and Hall effects. They did not discuss the irregular heat source and chemical reaction in their model. Here in the present study, we investigate the nanofluid flow in a rotating channel with the addition of an irregular heat source and a chemical reaction. For the confirmation of our results, we compare it with the results obtained by Tili et al. [55]. By ignoring the irregular heat source and chemical reaction, it is confirmed that our solution exactly matched the results provided by Tili et al. [55] up to the five decimal places. The key points of the present study are summarized below:

- It is observed that the velocity profiles decline with the increasing values of the suction factor;
- The velocity profile increases when the values of the rotation factor are increased;
- The temperature field exhibits a rising behavior for increasing values of the thermophoresis factor, Brownian motion, and thermal radiation factor;
- The concentration profile decreases when the values of Brownian and thermophoresis numbers are increased;
- It is analyzed that the concentration field declines with the variation of Sc and δ.
- Shear stress at the upper wall increases when the rotation variable and suction variable are amplified;
- Heat transmission escalates at the bottom wall when Pr, Rd, and d are increased.

The study can be enhanced by including the Hall current and ion-slip effects to any viscoelastic non-Newtonian model. The non-Newtonian models have a wide range of applications in the fluid flow. Additionally, simple thermal radiation can be replaced with nonlinear thermal radiation, and a gyrotactic microorganism effect can be added.

Author Contributions: Conceptualization, Z. and N.A.S.; methodology, N.A.A.; software, A. and H.U.R.; validation, J.D.C., A. and H.U.R.; formal analysis, N.A.A.; investigation, A.; resources, H.U.R.; data curation, N.A.A.; writing—original draft preparation, Z. and N.A.S.; writing—review and editing, J.D.C.; visualization, Z.; funding acquisition, J.D.C. All authors have read and agreed to the published version of the manuscript.

Data Availability Statement: The data presented in this study are available upon request from the corresponding authors.

Conflicts of Interest: The authors declared no conflict of interest.

References

1. Choi, S.U.; Eastman, J.A. *Enhancing Thermal Conductivity of Fluids with Nanoparticles*; No. ANL/MSD/CP-84938, CONF-951135-29; Argonne National Lab.: Lemont, IL, USA, 1995.
2. Buongiorno, J. Convective transport in nanofluids. *J. Heat Transfer* **2006**, *128*, 240–250. [CrossRef]
3. Rafati, M.; Hamidi, A.A.; Niaser, M.S. Application of nanofluids in computer cooling systems (heat transfer performance of nanofluids). *Appl. Therm. Eng.* **2012**, *45–46*, 9–14. [CrossRef]
4. Xian, H.W.; Sidik, N.A.C.; Najafi, G. Recent state of nanofluid in automobile cooling systems. *J. Therm. Anal. Calorim.* **2019**, *135*, 981–1008. [CrossRef]

5.	Sheikhpour, M.; Arabi, M.; Kasaeian, A.; Rokn Rabei, A.; Taherian, Z. Role of nanofluids in drug delivery and biomedical technology: Methods and applications. *Nanotechnol. Sci. Appl.* **2020**, *13*, 47–59. [CrossRef] [PubMed]

6.	Nagarajan, P.K.; Subramani, J.; Suyambazhahan, S.; Sathyamurthy, R. Nanofluids for solar collector applications: A review. *Energy Procedia* **2014**, *61*, 2416–2434. [CrossRef]

7.	Motsumi, T.G.; Makinde, O.D. Effects of thermal radiation and viscous dissipation on boundary layer flow of nanofluids over a permeable moving flat plate. *Phys. Scr.* **2012**, *86*, 045003. [CrossRef]

8.	Saidur, R.; Leong, K.Y.; Mohammed, H.A. A review on applications and challenges of nanofluids. *Renew. Sustain. Energy Rev.* **2011**, *15*, 1646–1668. [CrossRef]

9.	Wong, K.V.; De Leon, O. Applications of nanofluids: Current and future. *Adv. Mech. Eng.* **2010**, *2*, 519659. [CrossRef]

10.	Sandeep, N.; Ashwinkumar, G.P. Impact of nanoparticle shape on magnetohydrodynamic stagnation-point flow of carreau nanoliquid: A comparative study. *Proc. Inst. Mech. Eng. Part E J. Process Mech. Eng.* **2021**, *236*, 1004–1012. [CrossRef]

11.	Sandeep, N.; Ranjana, B.; Samrat, S.P.; Ashwinkumar, G.P. Impact of nonlinear radiation on magnetohydrodynamic flow of hybrid nanofluid with heat source effect. *Proc. Inst. Mech. Eng. Part E J. Process Mech. Eng.* **2022**, *236*, 1616–1627. [CrossRef]

12.	Samrat, S.P.; Ashwinkumar, G.P.; Sandeep, N. Simultaneous solutions for convective heat transfer in dusty-nano-and dusty-hybrid nanoliquids. *Proc. Inst. Mech. Eng. Part E J. Process Mech. Eng.* **2021**, *236*, 473–479. [CrossRef]

13.	Chalavadi, S.; Madde, P.; Naramgari, S.; Gangadhar Poojari, A. Effect of variable heat generation/absorption on magnetohydrodynamic sakiadis flow of casson/carreau hybrid nanoliquid due to a persistently moving needle. *Heat Transfer.* **2021**, *50*, 8354–8377. [CrossRef]

14.	Mabood, F.; Ashwinkumar, G.P.; Sandeep, N. Effect of nonlinear radiation on 3D unsteady MHD stagnancy flow of Fe3O4/graphene–water hybrid nanofluid. *Int. J. Ambient Energy* **2020**, *43*, 3385–3395. [CrossRef]

15.	Mabood, F.; Ashwinkumar, G.P.; Sandeep, N. Simultaneous results for unsteady flow of MHD hybrid nanoliquid above a flat/slendering surface. *J. Therm. Anal. Calorim.* **2021**, *146*, 227–239. [CrossRef]

16.	Tlili, I.; Nabwey, H.A.; Ashwinkumar, G.P.; Sandeep, N. 3-D magnetohydrodynamic AA7072-AA7075/methanol hybrid nanofluid flow above an uneven thickness surface with slip effect. *Sci. Rep.* **2020**, *10*, 4265. [CrossRef]

17.	Nehad, A.S.; Abderrahim, W.; Essam, R.E.; Thirupathi, T.; Se-Jin, Y.; Ashwinkumar, G.P. Heat transfers Thermodynamic activity of a second-grade ternary nanofluid flow over a vertical plate with Atangana-Baleanu Time-Fractional integral. *Alex. Eng. J.* **2022**, *12*, 10045–10053.

18.	Raju, C.S.K.; Ameer, N.A.; Kiran, S.; Nehad, A.S.; Se-jin, Y.; Dinesh, M.K. Nonlinear linear movements of axisymmetric ternary hybrid nanofluids in a thermally radiated expanding or contracting permeable Darcy Walls with different shapes and densities: Simple linear regression. *Int. Commun. Heat Mass Transfer* **2022**, *135*, 106110. [CrossRef]

19.	Ghulam, R.; Nehad, A.S.; Essam, R.E.; Abderrahim, W. Numerical investigation of EMHD nanofluid flows over a convectively heated riga pattern positioned horizontally in a porous medium: Application of passive control strategy and generalized transfer laws. *Waves Random Complex Media* **2022**, 1–20.

20.	Tlili, I.; Nabwey, H.A.; Samrat, S.P.; Sandeep, N. 3D MHD nonlinear radiative flow of CuO-MgO/methanol hybrid nanofluid beyond an irregular dimension surface with slip effect. *Sci. Rep.* **2020**, *10*, 1–14. [CrossRef]

21.	Alotaibi, H.; Althubiti, S.; Eid, M.R.; Mahny, K.L. Numerical treatment of mhd flow of casson nanofluid via convectively heated non-linear extending surface with viscous dissipation and suction/injection effects. *Comput. Mater. Continua* **2020**, *66*, 229–245. [CrossRef]

22.	Yu, B.; Ramzan, M.; Riasat, S.; Kadry, S.; Chu, Y.M.; Malik, M.Y. Impact of autocatalytic chemical reaction in an Ostwald-de-Waele nanofluid flow past a rotating disk with heterogeneous catalysis. *Sci. Rep.* **2021**, *11*, 15526. [CrossRef] [PubMed]

23.	Shaheen, N.; Ramzan, M.; Alshehri, A.; Shah, Z.; Kumam, P. Soret–Dufour impact on a three-dimensional Casson nanofluid flow with dust particles and variable characteristics in a permeable media. *Sci. Rep.* **2021**, *11*, 14513. [CrossRef] [PubMed]

24.	Bilal, M.; Ramzan, M.; Mehmood, Y.; Kbiri Alaoui, M.; Chinram, R. An entropy optimization study of non-Darcian magnetohydrodynamic Williamson nanofluid with nonlinear thermal radiation over a stratified sheet. *Proc. Inst. Mech. Eng. Part E J. Process Mech. Eng.* **2021**, *235*, 1883–1889. [CrossRef]

25.	Liu, C.; Khan, M.U.; Ramzan, M.; Chu, Y.M.; Kadry, S.; Malik, M.Y.; Chinram, R. Nonlinear radiative Maxwell nanofluid flow in a Darcy–Forchheimer permeable media over a stretching cylinder with chemical reaction and bioconvection. *Sci. Rep.* **2021**, *11*, 9391. [CrossRef]

26.	Bashir, S.; Ramzan, M.; Chung, J.D.; Chu, Y.M.; Kadry, S. Analyzing the impact of induced magnetic flux and Fourier's and Fick's theories on the Carreau-Yasuda nanofluid flow. *Sci. Rep.* **2021**, *11*, 9230. [CrossRef]

27.	Ma, Y.; Mohebbi, R.; Rashidi, M.M.; Yang, Z. Study of nanofluid forced convection heat transfer in a bent channel by means of lattice Boltzmann method. *Phys. Fluids* **2018**, *30*, 032001. [CrossRef]

28.	Zhang, Y.; Shahmir, N.; Ramzan, M.; Alotaibi, H.; Aljohani, H.M. Upshot of melting heat transfer in a Von Karman rotating flow of gold-silver/engine oil hybrid nanofluid with cattaneo-christov heat flux. *Case Stud. Therm. Eng.* **2021**, *26*, 101149. [CrossRef]

29.	Riasat, S.; Ramzan, M.; Sun, Y.L.; Malik, M.Y.; Chinram, R. Comparative analysis of Yamada-Ota and Xue models for hybrid nanofluid flow amid two concentric spinning disks with variable thermophysical characteristics. *Case Stud. Therm Eng.* **2021**, *26*, 101039. [CrossRef]

30.	Zeeshan; Rasheed, H.U.; Khan, W.; Khan, I.; Alshammari, N.; Hamadneh, N. Numerical computation of 3D Brownian motion of thin film nanofluid flow of convective heat transfer over a stretchable rotating surface. *Sci. Rep.* **2022**, *12*, 2708. [CrossRef]

31. Khan, Z.; Rasheed, H.U.; Khan, I.; Abu-Zinadah, H.; Aldahlan, M.A. Mathematical Simulation of Casson MHD Flow through a Permeable Moving Wedge with Nonlinear Chemical Reaction and Nonlinear Thermal Radiation. *Materials* **2022**, *15*, 747. [CrossRef]

32. Waini, I.; Ishak, A.; Pop, I. Hybrid nanofluid flow past a permeable moving thin needle. *Mathematics* **2020**, *8*, 612. [CrossRef]

33. Khan, I.; Weera, W.; Mohamed, A. Heat transfer analysis of Cu and Al2O3 dispersed in ethylene glycol as a base fluid over a stretchable permeable sheet of MHD thin-film flow. *Sci. Rep.* **2022**, *12*, 8878.

34. Ashraf, M.Z.; Rehman, S.U.; Farid, S.; Hussein, A.K.; Ali, B.; Weera, W. Insight into significance of bioconvection on MHD tangent hyperbolic nanofluid flow of irregular thickness across a slender elastic surface. *Mathematics* **2022**, *10*, 2592. [CrossRef]

35. Lou, Q.; Ali, B.; Rehman, S.U.; Habib, D.; Abdal, S.; Chung, J.D. Micropolar dusty fluid: Coriolis force effects on dynamics of MHD rotating fluid when lorentz force is significant. *Mathematics* **2022**, *10*, 2630. [CrossRef]

36. Abderrahmane, A.; Qasem, N.A.A.; Younis, O.; Marzouki, R.; Mourad, A.; Chung, J.D. MHD hybrid nanofluid mixed convection heat transfer and entropy generation in a 3-D triangular porous cavity with zigzag wall and rotating cylinder. *Mathematics* **2022**, *10*, 769. [CrossRef]

37. Abbas, N.; Nadeem, S.; Saleem, A.; Malik, M.Y.; Issakhov, A.; Alharbi, F.M. Models base study of inclined MHD of hybrid nanofluid flow over nonlinear stretching cylinder. *Chin. J. Phys.* **2021**, *69*, 109–117. [CrossRef]

38. Fourier, J.; Baptiste, J. *Théorie Analytique de la Chaleur*; Chez Firmin Didot, père et fils: Paris, France, 1822.

39. Cattaneo, C. Sulla conduzione del calore. *Atti. Sem. Mat. Fis. Univ. Modena* **1948**, *3*, 83–101.

40. Christov, C.I. On frame indifferent formulation of the Maxwell–Cattaneo model of finite-speed heat conduction. *Mech. Res. Commun.* **2009**, *36*, 481–486. [CrossRef]

41. Zeeshan; Ahammad, N.A.; Rasheed, H.U.; El-Deeb, A.A.; Almarri, B.; Shah, N.A. A Numerical Intuition of Activation Energy in Transient Micropolar Nanofluid Flow Configured by an Exponentially Extended Plat Surface with Thermal Radiation Effects. *Mathematics* **2022**, *10*, 4046. [CrossRef]

42. Rehman, S.; Zeeshan; Rasheed, H.U.; Islam, S. Visualization of multiple slip effects on the hydromagnetic Casson nanofluid past a nonlinear extended permeable surface: A numerical approach. *Waves Random Complex Media* **2022**, 1–18. [CrossRef]

43. Li, J.; Zheng, L.; Liu, L. MHD viscoelastic flow and heat transfer over a vertical stretching sheet with Cattaneo-Christov heat flux effects. *J. Mol. Liq.* **2016**, *221*, 19–25. [CrossRef]

44. Shehzad, S.A.; Abbasi, F.M.; Hayat, T.; Ahmad, B. Cattaneo-Christov heat flux model for third-grade fluid flow towards exponentially stretching sheet. *Appl. Math. Mech.* **2016**, *37*, 761–768. [CrossRef]

45. Rehman, S.U.; Fatima, N.; Ali, B.; Imran, M.; Ali, L.; Shah, N.A.; Chung, J.D. The Casson Dusty Nanofluid: Significance of Darcy–Forchheimer Law, Magnetic Field, and Non-Fourier Heat Flux Model Subject to Stretch Surface. *Mathematics* **2022**, *10*, 2877. [CrossRef]

46. Sui, J.; Zheng, L.; Zhang, X. Boundary layer heat and mass transfer with Cattaneo–Christov double diffusion in upper-convected Maxwell nanofluid past a stretching sheet with slip velocity. *Int. J. Therm. Sci.* **2016**, *104*, 461–468. [CrossRef]

47. Acharya, N.; Das, K.; Kundu, P.K. Cattaneo–Christov intensity of magnetised upper-convected Maxwell nanofluid flow over an inclined stretching sheet: A generalised Fourier and Fick's perspective. *Int. J. Mech. Sci.* **2017**, *130*, 167–173. [CrossRef]

48. Nagendramma, V.; Raju, C.S.K.; Mallikarjuna, B.; Shehzad, S.A.; Leelarathnam, A. 3Dcasson nanofluid flow over slendering surface in a suspension of gyrotactic microorganisms with Cattaneo-Christov heat flux. *Appl. Math. Mech.* **2018**, *39*, 623–638. [CrossRef]

49. Rauf, A.; Mushtaq, A.; Shah, N.A.; Botmart, T. Heat transfer and hybrid ferrofluid flow over a nonlinearly stretchable rotating disk under the influence of an alternating magnetic field. *Sci. Rep.* **2022**, *12*, 17548. [CrossRef]

50. Ullah, K.S.; Ali, N.; Hayat, T.; Abbas, Z. Heat transfer analysis based on Cattaneo-Christov heat flux model and convective boundary conditions for flow over an oscillatory stretching surface. *Therm. Sci.* **2019**, *23*, 443–455. [CrossRef]

51. Lv, Y.P.; Gul, H.; Ramzan, M.; Chung, J.D.; Bilal, M. Bioconvective Reiner–Rivlin nanofluid flow over a rotating disk with Cattaneo–Christov flow heat flux and entropy generation analysis. *Sci. Rep.* **2021**, *11*, 15859. [CrossRef]

52. Abid, N.; Ramzan, M.; Chung, J.D.; Kadry, S.; Chu, Y.M. Comparative analysis of magnetized partially ionized copper, copper oxide–water and kerosene oil nanofluid flow with Cattaneo–Christov heat flux. *Sci. Rep.* **2020**, *10*, 19300. [CrossRef]

53. Li, Y.X.; Shah, F.; Khan, M.I.; Chinram, R.; Elmasry, Y.; Sun, T.C. Dynamics of cattaneo- Christov double diffusion (CCDD) and arrhenius activation law on mixed convective flow towards a stretched Riga device. *Chaos Solitons Fractals* **2021**, *148*, 111010. [CrossRef]

54. Ramzan, M.; Gul, H.; Kadry, S.; Chu, Y.M. Role of bioconvection in a three dimensional tangent hyperbolic partially ionized magnetized nanofluid flow with cattaneo-Christov heat flux and activation energy. *Int. Commun. Heat Mass Transfer* **2021**, *120*, 104994. [CrossRef]

55. Tlili, I.; Hamadneh, N.N.; Khan, W.A.; Atawneh, S. Thermodynamic analysis of MHD Couette-Poiseuille flow of water-based Nano fluids in a porous channel with radiation and Hall effects. *J. Term. Anal. Calorim.* **2018**, *132*, 1899–1912. [CrossRef]